Article:
Liu, H., Pasqua, A., Nichols, H. et al. (2026) Effects of grain size on landslide–forest interaction. Engineering Geology, 364. 108613. ISSN: 0013-7952

https://doi.org/10.1016/j.enggeo.2026.108613

Effects of grain size on landslide–forest interaction

Haiming Liu[1*]; Andrea Pasqua[1]; Hannah Nichols[1]; Alessandro Leonardi[1]

[1]School of Mechanical, Aerospace and Civil Engineering, University of Sheffield, Sheffield, United Kingdom
*Corresponding author, email address: haiming.liu@sheffield.ac.uk

Abstract

Forests play an essential but poorly-understood role in mitigating landslide runout by providing mechanical resistance and dissipating flow energy. Despite growing interest, existing models treat forests as friction modifiers or generic porous obstacles, and largely ignore how grain size controls retention and jamming. This study experimentally investigates and resolves the influence of grain size, slope angle, and tree spacing on landslide–forest interactions using reduced-scale flume tests with different granular materials. Results show that although forests can reduce flow mobility, preferential flow paths may develop along trees, leading to ineffective energy dissipation along the flow flanks. For fine-grained flows composed of sand, the deposition behaviour is governed by the normalised slope angle and the transverse blockage ratio. For coarse-grained flows composed of gravel, the deposition and retention are controlled by two distinct jamming mechanisms: frontal deposit-induced jamming and arching-induced jamming. Frontal deposit-induced jamming occurs in all jamming cases, whereas arching-induced jamming only develops when tree spacing is smaller than three times of the grain size. We capture this variety of phenomena within two phase diagrams for fine-grained and coarse-grained flows. The phase diagrams provide a direct screening rule for minimum tree density and slope condition required to ensure jamming for a given grain size distribution.

Keywords: landslide–forest interaction; landslides; grain size; retention efficiency; jamming; nature-based solution

Highlights

- Laboratory tests reveal grain size-dependent mechanisms in landslide–forest interaction.
- An improperly patterned forest may facilitate a preferential flow path at flow flanks, resulting in inefficient impedance on landslide mobility.

- Two phase diagrams are proposed with defined retention regimes for fine-grained and coarse-grained landslides, serving as a basis for nature-based mitigation design.

Introduction

Landslides are among the most frequent and destructive geological hazards in mountainous regions worldwide, posing severe threats to human lives and infrastructure (Froude and Petley 2018). Their frequency and magnitude are projected to increase under the combined influences of climate change and deforestation (Stoffel et al. 2014; Nicoll 2016; Fidan et al. 2024; Yanites et al. 2025). Conventional engineering countermeasures, such as rigid and flexible barriers, are effective in controlling landslide runout distance but are often costly to construct and maintain, and can impose considerable disturbance to fragile mountain environments (Ng et al. 2020; Zhang et al. 2024; Pasqua et al. 2025). In contrast, forests offer a sustainable and nature-based alternative that can mitigate against landslides, while further offering multiple ecological benefits. Field observations have shown that forests can contribute to resisting landslide runout by acting as a natural physical barrier (Booth et al. 2020; Perzl et al. 2021). However, the underlying mechanisms governing the interaction between landslides and forests remain insufficiently understood. Advancing this understanding is essential for developing reliable models to guide sustainable slope management, hazard mitigation, and afforestation strategies in mountain regions.

Extensive research has clarified the role of vegetation in stabilizing slopes prior to failure, emphasizing hydrological effects and benefits of mechanical reinforcement from roots. In recent years, growing attention has been directed towards how forests interact with, and decelerate the runout of flowing landslides. Noted that in this paper, the term “landslide” serves as an umbrella term for rapid mass movements on slopes, “granular flow” refers to dry grain-dominated flows, and “debris flow” refers specifically to two-phase flow with soil and a significant water component.

Luong et al. (2020) experimentally investigated the spreading dynamics of landslides, simulated as a granular flow impacting against an array of rigid tree elements. They found that the presence of trees induces lateral spreading and reduces flow velocity. This spread-out and slow-down effect was further quantified through an empirical law incorporating the influences of slope angle, landslide magnitude, and tree spacing. Cui and Gray (2013) and Khan et al. (2020) investigated the bow shock formation and interaction of granular flow impacting single and dual obstacles, respectively. Later, Liang et al. (2023) assessed the role of bow-shock interaction in the dynamics of granular flow impacting forests and studied the effects of stem diameter, tree spacing, and forest patterns on flow mobility. Their results revealed that overlapping bow shocks can either attenuate or enhance flow momentum, suggesting that classical models relying solely on modified basal friction (Benito et al. 2012; Darbois Texier et al. 2023) and should be applied with caution. Choi (2025) further reported numerical analyses to study the effects of tree failure on granular flow–forest interactions and emphasized the role of entrained tree elements in modifying flow mobility. These recent studies model forests using cylindrical rods, much like earlier investigations conducted on landslide impact and interaction with baffles, which are arrays of artificial obstacles, however these use fewer rows than a model forest (Choi et al. 2014; Ng et al. 2015).

Despite recent advances in understanding landslide–forest interaction mechanisms, most studies have simplified landslide material by using fine grains with particle sizes comparable to sand, thereby neglecting the influence of grain size. However, grain size plays a fundamental role in controlling landslide mobility (Cagnoli 2024) and the impact dynamics against engineering structures by altering the stress distribution within the flow (Cui et al. 2018). For slit-type barriers (Choi et al. 2016; Leonardi et al. 2019; Goodwin and Choi, 2020; Marchelli et al. 2020; Piton et al. 2022; Kong and Guan, 2023), a smaller ratio of slit opening to grain size reduces the discharge

rate and may even trigger jamming. Here, jamming is defined as a transition from a flowing to a static state caused by grain interlocking and friction (To et al. 2001; Jerolmack and Daniels, 2019).

Similar effects occur in forested terrains, where the altered discharge dynamics and potential jamming can significantly affect the mobility and retention of landslides containing coarse grains. Field observations of landslides that occurred in Scotland, UK, in July 2023 illustrate this phenomenon. Five of the triggered landslides developed into debris flows, three of which blocked the road. All flows travelled through forested areas before discharging onto the road. Boulder-sized grains were observed to accumulate behind individual trees (Fig. 1a) and even more extensively between multiple trees (Fig. 1b). An increase in tree density appears to enhance the deposition of coarse material by promoting jamming, analogous to the physical processes observed in hopper flow (Nedderman 1992; To et al. 2001). Therefore, understanding the influence of grain size is critical for evaluating the capacity of forest in mitigating landslides.

These effects are rarely observed in the field, as small landslides occurring within forests are largely unreported, highlighting the need for physical modelling under controlled conditions. Therefore, this paper aims to study the effects of grain size on landslide–forest interactions through a series of controlled flume experiments. This study addresses three main questions. First, under which combinations of slope angle, tree density and grain size do forests retain or jam landslides, and under which conditions do they fail to do so. Second, how do these retention regimes differ between flows dominated by fine grains and those dominated by coarse grains. Third, how can these regimes be expressed in a simple form that can support the design and assessment of nature-based mitigation strategies. To answer these questions, we propose experiments that examine the impact kinematics, flow mobility, retention capacity, and jamming behaviour of landslides interacting with forests. Based on the experimental results, new design diagrams are proposed to

characterise landslide jamming induced by forests, providing both a scientific basis and practical reference for analysing landslide–forest interactions.

Similar to the previous studies on landslide–forest interaction (Benito et al. 2012; Luong et al. 2020; Liang et al. 2023; Darbois Texier et al. 2023; Choi 2025), the landslide material is represented as a dry granular assembly in this study. Iverson et al. (2004) performed a scaling analysis of granular flows in small-scale experiments. They showed that when flow is dry, the influence of intergranular fluid and cohesion is negligible, which leads to less pronounced scale effects. Accordingly, the results from this study may be directly applicable to dry granular flows in the field. In two-phase debris flows, both the solid and fluid phases influence the overall dynamics (Iverson 1997). However, grain-size segregation commonly leads to coarse-particle enrichment at the debris-flow snout and along levees, where pore-water pressures tend to be low (Johnson et al. 2012). In these regions, frictional and collisional grain interactions dominate and can strongly influence deposition by providing much of the resisting stress acting on the flow body. Consequently, dry granular deposition processes can offer useful insight into the depositional behaviour of two-phase debris flows.

Physical modelling of landslide–forest interaction

Experimental setup

Fig. 2 shows a schematic of the experimental setup, which consists of a rigid inclined plane and a storage container made of transparent acrylic plates, and an aluminium collection bin. The inclined plane is supported by an aluminium frame that allows adjustment over a wide range of slope angles. The inclined plane has a width of 600 mm and a length of 900 mm, with two acrylic sidewalls installed to confine the flow. To reduce basal slip, sandpaper with a grit size of P120 was attached

to the plane surface to achieve an interface friction comparable to the internal friction of the granular material. An array of rigid plastic cylindrical rods were mounted on the plane to model forest trees. The rods were arranged in a regular hexagonal pattern, in which the smallest spacing between adjacent trees was defined as s. In this configuration, the centre-to-centre longitudinal spacing (s*) of two trees along the slope was $\sqrt{3}(s + D)$, where D denotes the tree diameter. This arrangement serves as a regular staggered pattern and is commonly adopted by previous studies (Luong et al. 2020; Védrine et al. 2022; Liang et al. 2023). The storage container, measuring 500 mm in height with an internal cross-section of 97 mm × 97 mm, was connected to the upper end of the inclined plane. The container was equipped with a double-gate release system to control the opening height and discharge of material. The collection bin was used to collect and measure the mass (M_2) of the material that was not retained by the forest. The measured discharged mass served to determine the retention mass (M_1) by the forest.

A high-speed camera was installed above the flow to capture the impact kinematics of landslide against the forest at 300 frames per second. Due to the recording duration of the high-speed camera being insufficient to capture the full flow until deposition for all the cases, an additional video camera operating at 120 frames per second was used to record the entire process from impact to final deposition. A second video camera, also at 120 frames per second, was mounted to capture the side view for obtaining the flow depth.

It should be noted that the forest in this study was idealised as arrays of rigid cylindrical obstacles, and the landslide–forest interaction was assumed to be governed solely by mechanical impacts between the flowing granular mass and these rigid cylindrical elements. In natural forests, however, tree stiffness, tree failure, and root systems can also play important roles in landslide dynamics. Variations in tree stiffness may lead to different energy-dissipation mechanisms within the flowing

mass, as reported for flexible barriers (Song et al. 2019). Entrainment of failed trees may increase internal frictional shearing within the flow, thereby reducing landslide mobility (Booth et al. 2020). In addition, roots can reinforce the soil and stabilise the erodible bed, potentially reducing landslide mobility (van den Broek et al. 2026). Further investigation using a more realistic experimental setup is therefore warranted.

Test programme

Dry granular materials with uniform angular grains were used to study the effects of grain size on landslide–forest interactions. Three grain sizes were adopted, which were sand with a mean grain size of 0.15 mm and gravels with mean grain sizes of d = 4 mm and 7 mm. The sand, 4-mm gravel, and 7-mm gravel had initial bulk densities of 1620, 1550, and 1470 kg/m^3, respectively, and corresponding angles of repose (φ) of 33°, 36°, and 36°. The angles of repose were determined by piling the grains on a flat surface until the maximum stable slope angle was reached. The angle of repose for the sand was similar to the interface friction angle between the sand and the sandpaper because the sandpaper grit size was chosen to be similar to the sand grain size. From this point forward the term "fine-grained" will refer to flows containing majority sand particles, whereas "coarse-grained" refers to majority gravel particle flows.

A total granular mass of 5 kg, a tree diameter of D = 20 mm, a tree height of 50 mm, and tree spacings of s = 20, 40, and 60 mm were adopted. These parameters were the same as those used by Luong et al. (2020). Since trees were simplified as rigid cylinders, the tree height was chosen pragmatically to prevent overflow. For tree diameter and spacing, the normalised tree diameter with respect to the coarse grain size (D/d) ranged from 3 to 5, and the normalised tree spacing (s/d) ranged from 2.9 to 15.0. Both ranges were consistent with field observations (Fig. 1). A similar experimental design rationale was also reported by Jan et al. (2025b).

Before conducting the landslide–forest interaction tests, control experiments without any tree elements were performed to characterise the flow behaviour. These control tests started at a slope inclination of 28° and increased in 2° increments until a critical inclination was reached at which the flume could no longer retain the flow. Since the slope itself can retain most of the flow material below this critical inclination, the experiments were designed with an inclination close to or larger than this angle to better consider forest effect. The critical inclinations for sand, 4-mm gravel, and 7-mm gravel are 34°, 30°, and 30°, respectively. Accordingly, four slope angles (θ = 32°, 36°, 40°, and 45°) were selected to enable the deposition process was predominantly governed by the confinement from the forest. The only exception was sand at θ = 32°, where basal friction played a dominant role in sand retention. The four slope angles (θ = 32°, 36°, 40°, and 45°) were corresponding to normalised slope angles (θ/φ) of 1.0, 1.1, 1.2, and 1.4 for sand, and 0.9, 1.0, 1.1, and 1.3 for gravel.

Scaling and flow characterisation

The Froude number (Fr), defined as the ratio of flow inertia force to gravitational force, is commonly used to achieve dynamic similarity in open-channel flows to characterise landslide interactions with various structures (Choi et al. 2016; Leonardi et al. 2019; Kong et al. 2021; Song et al. 2021; Cui et al. 2022; Fang et al. 2023). The Froude number is expressed as:

$$Fr = \frac{v}{\sqrt{gh\cos\theta}} \tag{1}$$

where v is the flow velocity (m/s), g is the gravitational acceleration (m/s^2), h is the flow depth, and θ is the slope angle (°). Control tests without any tree element were carried out to determine the flow velocity and flow depth of the unobstructed flow at the four selected slope angles (θ = 32°, 36°, 40°, and 45°). The values were taken at the location of the initial impact with the first

row of trees. The flow velocity immediately upstream of the first tree row was obtained by averaging the flow velocity from release to a point 200 mm downstream of the gate, which was twice the distance between the gate and the first tree row. Assuming a linear increase in velocity over this reach, the average value provides an estimate of the instantaneous velocity just before impact with the first tree row (Jan et al. 2025a). The maximum flow depth at the first row of the trees was determined from side-view images captured by the video camera. In the control tests, the measured Froude numbers ranged narrowly from 2.1 to 2.7, which were representative of typical landslide observed in the field (Zhou et al. 2019).

Another dimensionless number, the Savage number (N_{Sav}), is adopted to characterise grain-grain interactions. N_{Sav} quantifies the ratio of grain collisional stresses to frictional stresses, and is expressed as follows (Savage and Hutter 1989; Iverson 1997):

$$N_{\mathrm{Sav}} = \frac{\dot{\gamma}^2 d^2}{gh\cos\theta\tan\varphi} \tag{2}$$

where $\dot{\gamma}$ is the shear rate (/s) and is estimated by assuming a linear velocity profile with the basal velocity taken as half of the surface velocity, following Johnson et al. (2012). The flow velocity and flow depth used to determine N_{Sav} are the same as those for the Froude number. The resulting N_{Sav} is approximately 2×10^{-6} for sand and ranges from 0.10 to 0.26 for gravels, indicating that the fine-grained and coarse-grained flows considered here lie predominantly in the frictional and collisional regimes, respectively.

Interpretation of test results

Observed impact kinematics

Fig. 3 illustrates the typical impact kinematics of a landslide interacting with a forest, recorded using the high-speed camera. The forest model is installed on a slope inclined at 32°, with a tree spacing of 60 mm, and the landslide materials are sand (Fig. 3a), 4-mm gravel (Fig. 3b), and 7-mm gravel (Fig. 3c). Flow velocity vectors are superimposed on the captured images through particle image velocimetry (PIV) analysis using the open-source MATLAB-based software PIVlab (Thielicke, 2014; Thielicke and Stamhuis, 2014), enabling visualisation of the variations in velocity fields induced by grain size. Regions without granular flow and those containing only isolated grains are excluded from the PIV analysis to ensure a clear and representative velocity field. Based on the PIV results, the mean flow velocities along the flow centreline, delineated by rectangular regions, are determined.

The time t = 0.00 s corresponds to the opening of the gate. For fine-grained flow (Fig. 3a), at t = 0.67 s, the flow interacts with the forest, forming bow shocks (Cui and Gray 2013; Liang et al. 2023) and spreading laterally. The flow velocity along the centreline gradually decreases with increasing downslope distance. The flow front along the centreline propagates faster than the flow flanks, due to greater energy dissipation in the spreading process. At t = 1.67 s, the spreading area further enlarges, and the central flow velocity continues to decrease with travel distance, indicating enhanced energy dissipation as the flow area expands. By t = 22.69 s, the fine-grained flow has completely ceased and deposited along the slope.

For the coarse-grained flow (4-mm gravel; Fig. 3b), the travel distance is shorter than that of the fine-grained flow at the same propagation time (t = 0.67 s). Meanwhile, the flow front along the

centreline does not exhibit noticeably faster propagation than the flank in contrast to the fine-grained case. The shorter travel distance may be attributed to the one-order-of-magnitude reduction in the ratio of tree spacing to grain size (s/d) compared with the fine-grained case, resulting in a lower discharge rate (Nedderman 1992) for coarse-grained flow. At t = 1.67 s, the spreading area increases, while the flow velocity along the centreline decreases compared with t = 0.67 s. In contrast to the continuously decreasing velocity trend along travel distance as observed in the fine-grained flow (Fig. 3a), the central flow velocity for the coarse grains first decreases and then re-accelerates. This re-acceleration near the flow front is mainly caused by more intensive grain collisions relative to the main flow body, leading to a more dilute front that propagates downslope with reduced frictional resistance. At t = 8.33 s, the main flow body is retained by the forest with negligible flow velocity. Meanwhile, the area of the retained flow body decreases as some grains within the flow body continue to detach from the bulk flow. This is mainly due to the larger ratio between tree spacing and grain size (s/d = 15.0), where the trees fail to provide sufficient resistance to stabilise the grains. The detached grains further impede the formation of stable deposits behind trees. Ultimately, nearly all grains pass through the forest, with only 3% of the initial mass retained by the tree array.

For the coarse-grained flow composed of much larger grains (7-mm gravel; Fig. 3c), an even shorter travel distance than that of the 4-mm gravel is observed at t = 0.67 s. The flow fronts at the centre and flank propagate over comparable distances, consistent with the behaviour shown in Fig. 3b. At t = 1.67 s, a similar variation in flow velocity is observed, although with a lower overall magnitude than in the 4-mm gravel case. By t = 14.42 s, all flow material is arrested by the forest. Owing to the decreased ratio between tree spacing and grain size (s/d = 8.6), the retained material is more stable than that of the 4-mm gravel due to the stronger force chain (Zhou et al. 2020).

Consequently, flow jamming occurs due to frontal deposits behind the trees, as indicated in the zoomed-in region. However, these frontal deposits can be disturbed during the test by impacts from subsequent grains. Once disturbed, the upstream material was re-mobilised until a new deposit capable of supporting the upstream grains was re-established. This process is referred to in this study as frontal deposit-induced jamming. The observed re-mobilisation suggests that stable arching did not form due to the larger ratio between tree spacing and particle size (s/d = 8.6) compared with the typical spacing required for open-type structures ($s/d \leqslant 3$) (Choi et al. 2016, 2020; Goodwin and Choi, 2020; Marchelli et al. 2020) and for hopper flows ($s/d \leqslant 6$) (Nedderman 1992). In contrast, arching-induced jamming was also observed when $s/d < 3$, where the development of force chains between grains and adjacent trees provides sufficient resistance to arrest the upstream material. The two jamming mechanisms are discussed in Fig. 11.

The observed impact kinematics indicate that grain size exerts a significant influence on landslide–forest interactions. The ratio of tree spacing to grain size (s/d) governs the discharge dynamics and deposition behaviour, thereby affecting the flow front propagation, lateral spreading, and retention capacity of the forest.

Flow front propagation

As shown in Fig. 3, the flow front does not always propagate the fastest along the centreline. To investigate the mechanism governing the relative spreading speeds of the lateral and central flow, the interaction between the fine-grained flow and the forest is examined, as the flow front of sand is easier to distinguish than gravel.

Fig. 4 shows the observed flow-front propagation captured by a video camera for fine-grained flows on a 45° slope with tree spacings of 20 mm (Fig. 4a), 40 mm (Fig. 4b), and 60 mm (Fig. 4c).

For forests with tree spacings of 20 mm and 40 mm, the lateral flow propagates faster than the central flow, despite the additional energy dissipation associated with lateral spreading. This enhanced lateral propagation occurs because the bow shocks formed along the flow flanks do not effectively interact with the downstream trees. As indicated in the enlarged regions, only a small portion of the bow shock impacts on the downstream trees, while a large portion travels further downslope through the tree spacing, approximately parallel to a diagonally aligned row of trees. In contrast, for the forest with a 60-mm spacing, the laterally formed bow shocks interact effectively with the downstream trees. The bow shock shown in an enlarged region at the flow front exhibits comparable dimensions on both sides of the tree, implying that the tree dissipates the kinetic energy of the lateral flow more efficiently by effectively interacting with the flow. The combined effects of energy dissipation from tree impacts and lateral spreading lead to reduced flow mobility along the flanks.

The results indicate that regularly patterned forests can, under certain conditions, promote the development of preferential flow paths around trees. This occurs when the bow shocks generated along the flow flanks fail to interact effectively with the downstream trees (Figs. 4a, 4b). The geometrical parameters of bow shock can be estimated by incoming flow velocity, material properties, tree diameter, and slope angle using an analytical equation proposed by Liang et al. (2023). However, this equation was derived for bow-shock formation around a single tree. Further investigation is therefore needed to quantify how bow-shock interactions in multi-row configurations modify the bow-shock angle, and how this can be used to guide tree arrangements that minimise preferential flow paths. Alternatively, introducing a degree of spatial randomness (Védrine et al. 2022) into the forest pattern could also help disrupt these preferential paths and thereby enhance the overall energy-dissipation capacity of the forest. In the field, natural forest is

usually irregularly arranged. Therefore, preferential flow paths are less likely to occur. Nevertheless, a further quantitative assessment on controlled randomness in facilitating energy dissipation during landslide–forest interaction is warranted.

Fig. 5 shows the time histories of the flow-front distance from the gate under different transverse blockage ratios and slope angles. The transverse blockage (B) is commonly used to characterise the opening ratio of slit-type structures (Choi et al. 2016; Marchelli et al. 2020) and is defined as $B = s/(s+D)$. In this study, B is used to describe the effective opening ratio of a single row of trees. At a slope angle of 36° (Fig. 5a), the flow centre consistently propagates faster than the flow flanks. In the control case without trees, the flow front initially accelerates before reaching a nearly constant speed, as indicated by the linear portion of the curve. For the densest forest (B = 0.50), the flow decelerates immediately after interacting with the first tree row at a travel distance of around 120 mm, before stabilising at a lower constant speed. When the tree spacing increases (B = 0.67), the flow front follows a similar trajectory to the control case up to about 240 mm and then decelerates to a steady speed. For the most open configuration (B = 0.75), the flow front maintains nearly the same speed as the control case up to 480 mm, beyond which the flow front slows down slightly. Across all cases, the curves initially overlap with the no-forest case and begin to diverge at travel distances of approximately 120 mm, 240 mm, and 480 mm for B = 0.50, 0.67 and 0.75, respectively. For a steeper slope of 45° (Fig. 5b), the flow-centre curves exhibit a similar trend to those at 36°, but with a steeper gradient due to greater flow inertia. The divergence from the no-forest case occurs at larger travel distances, which are approximately 180 mm, 240 mm, and 660 mm for B = 0.50, 0.67, and 0.75, respectively, indicating the delayed onset of energy dissipation under higher inertial conditions.

These results suggest that the influence of the forest on flow deceleration becomes progressively delayed with decreasing transverse blockage and increasing slope angle, highlighting the combined role of tree spacing and flow inertia in governing the onset of energy dissipation. Moreover, the flow flanks for $B = 0.50$ (Fig. 4a) and 0.67 (Fig. 4b) travel faster than the flow centre. The flow flank at $B = 0.67$ maintains a nearly constant speed, while that at $B = 0.50$ decelerates with time, indicating that denser forests also promote more energy dissipation along the flow flanks.

To further quantify the influence of the forest on flow propagation along the centre and flanks, Fig. 6 compares the flow-front propagation time with the corresponding transverse blockage ratios. The flow-front propagation time for tests with forest (T_1) is normalised by the time required for the flow to traverse the same slope without trees (T_0), thereby reflecting the efficiency of the forest in decelerating the landslide. The slope angle (θ) is normalised by the angle of repose (φ). Solid symbols represent propagation along the flow centreline, whereas hollow symbols denote cases where the flow flanks propagate faster. Since intensive collisions among coarse grains hinder clear identification of the flow front, only fine-grained flows are analysed.

At a transverse blockage of $B = 0.50$, the flow-front propagation time is extended by up to an order of magnitude compared with the case on a bare slope. As B increases, the normalised propagation time at the flow centre for a slope angle of $\theta/\varphi = 1.1$ decreases more sharply than for steeper slopes, and the differences among slope angles become smaller. Lower slope angles result in a longer propagation time due to the lower inertia. This indicates the forests to be more effective at dissipating energy when the flow inertia is also low.

For comparison, the only available experimental measurements of flow-front propagation reported by Luong et al. (2020) at a slope angle of $\theta = 30°$ ($\theta/\varphi = 1.4$, where φ is estimated from the quasi-static internal friction angle from Jop et al. (2006)) are also included. Despite the similar

normalised slope angle, the normalised frontal propagation times from Luong et al. (2020) are up to 30% smaller than those observed in this study at B = 0.50 and 0.67. This discrepancy may be attributed to the smoother cork surface used by Luong et al. (2020), which provided less basal resistance and thus reduced the overall energy dissipation of the forest. The normalised propagation time along the flow flanks at B = 0.50 and 0.67 and θ/φ = 1.2 and 1.4 is lower than their flow centre by up to 60%, owing to the significantly reduced resistance provided by the forest to lateral flow motion. This limited forest impedance consistently leads to shorter propagation time at the flanks at steeper slopes, where flow inertia dominates.

Forest retention of fine-grained landslides

After examining the flow mobility, the deposition behaviour against the forest is analysed to better understand the retention capacity of a forest. Fig. 7 shows the final sand deposition patterns for tests with a transverse blockage ratio of 0.5 under different slope angles: θ = 36° (Fig. 7a), 40° (Fig. 7b), and 45° (Fig. 7c). A closer inspection of the deposition for θ = 36° and 45° (Figs. 6d and 6e, respectively) reveals a clear contrast in deposition extent, with the gentler slope (36°) producing a longer deposit and the steeper slope (45°) resulting in a shorter one. The deposition length (Figs. 6d, 6e) reflects the retention capacity of a forest.

At a slope angle of θ = 36° (Fig. 7a), deposits with long length form behind each tree, and the merging of these deposits produces a continuous deposition sheet along the slope. Since this slope angle exceeds both the angle of repose and the critical interface angle between the flow and the base, the extended deposition suggests that the forest provided additional resistance, enabling the formation of continuous deposition. This process is discussed in Fig. 9.

When the slope angle increases to θ = 40° (Fig. 7b), the deposition becomes shorter and more fragmented, resulting in a smaller overall deposition area compared with the gentler slope. Notably, the deposition lengths at the lateral sides of the forest are longer than those in the centre. Given that the slope angle and tree spacing are uniform across the slope, this non-uniform pattern can be attributed to the higher flow inertia at the centre, which enhances material mobility. This highlights the significant role of flow inertia in governing final deposition. At θ = 45° (Fig. 7c), the steep inclination yields a more uniformly distributed but shorter deposition. Comparison among the three slope angles reveals that both very gentle and very steep slopes promote a relatively uniform deposition pattern. This occurs because the slope angle becomes the dominant control and the difference in flow velocities between the centre and the flanks (Fig. 3a) has a negligible influence on the final deposition. In contrast, an intermediate slope tends to produce a non-uniform deposition pattern because the reduced flow kinetic energy along the flanks can be more effectively dissipated by the forest (Fig. 6). Consequently, flow along the flanks causes less disturbance to the forming deposits and results in longer deposition lengths compared with the flow centre.

To quantify the retention capacity of the forest, Fig. 8 compares the retention efficiency of sand by forests with different transverse blockage ratios and slope angles. The retention efficiency (E) is defined as the mass ratio between the material retained by the forest (M_1) and the total material (M) initially stored in the container, where M_1 is determined from the measured discharged mass (M_2) collected in the bin (Fig. 2). The expression for E is given as follows:

$$E = \frac{M_1}{M} = \frac{(M - M_2)}{M} \tag{3}$$

For a slope angle of 32°, the forest achieves full retention at B = 0.5 and 0.67 and retains 16% of the material at B = 0.75. When the slope angle increases to 36°, the overall retention efficiency

decreases in contrast to the gentler slope. A maximum efficiency of E = 57% is observed at B = 0.5, followed by a sharp reduction to 9% as B increases to 0.67. For steeper slopes of θ = 40° and 45°, only up to 5% of the material is retained, even for the densest forest configuration (B = 0.5). These results highlight the joint influence of slope angle and tree spacing on the retention efficiency and suggest the presence of threshold conditions beyond which a forest becomes ineffective in retaining fine-grained flow.

Phase diagram for fine-grained landslide deposition

As observed in the sand deposition patterns (Fig. 7), the ratio between the deposition length and a characterised tree spacing may be used to determine the threshold values of tree spacing and slope angle for characterising retention capacity. Fig. 9 shows an idealised schematic of deposition profiles of fine-grained flow against a tree. Noted that the deposition height H is defined as the length measured normal to the slope surface. In a global vertical coordinate system, the corresponding vertical height can be slightly larger. The side view (Fig. 9a) of the deposition profile indicates the condition with the largest deposition length (l) under a deposition height H and deposition angle equal to the angle of repose φ. Based on the geometric relationship, when the slope angle θ exceeds the angle of repose φ, the maximum deposition length can be expressed as follows:

$$l = \frac{H}{\tan(\theta - \varphi)} \tag{4}$$

Eq. (4) provides an overestimation on the deposition length by assuming a maximum deposition length achievable under an idealised two-dimensional condition. Based on the observations in Figs. 6d and 6e, the deposition height H can be estimated by assuming that the sand accumulates along

the front surface of the tree element with a width W and a deposition angle equal to the angle of repose φ (Fig. 9b). The expression is given as follows:

$$H = \frac{W}{2}\tan\varphi \tag{5}$$

Eq. (5) assumes that the tree stands on a horizontal plane. This assumption underestimates the deposition height because a sloping surface can provide additional resistance, leading to a larger deposition height. However, this underestimation is partly compensated by assuming a sufficiently rough cylinder surface, which overestimates the deposition height.

The width of the deposition is primarily controlled by the tree diameter, the angle of repose, and the interface friction angle between the sand and the tree surface. Fig. 9c shows a top view of the deposition along the surface of the cylindrical tree element. For simplicity, the tree is assumed to be installed on a vertical slope. Under this assumption, for a rough surface where the interface friction angle exceeds the angle of repose, the maximum deposition angle can be approximated as the angle of repose. Accordingly, the deposition width can be expressed as follows:

$$W = D\sin\varphi \tag{6}$$

It is noted that if the slope is not assumed to be vertical, the angle of the cone sediment on top of the circular cross-section of the tree element would exceed the angle of repose (Fig. 9c), resulting in a larger deposit width. Nevertheless, this underestimation is also partly compensated by the assumption of a sufficiently rough cylinder surface, which overestimates the width.

When the deposition length becomes sufficiently large such that the deposits formed behind adjacent trees in the longitudinal direction connect with each other (Fig. 7a), the overall deposition area can be considered continuous. Under this condition, the mobilisation of bed friction is maximised, resulting in effective flow retention. Accordingly, the deposition length should be no

less than the centre-to-centre tree spacing (s*) in the longitudinal direction (Fig. 2b) to reach the continuous deposition sheet, which can be expressed for this specific configuration as:

$$l \geq \sqrt{3}(s + D) \tag{7}$$

Substituting Eqs. (4) to (6) into Eq. (7) gives:

$$\frac{s + D}{D} \leq \frac{\sin\varphi \tan\varphi}{2\sqrt{3}\tan(\theta - \varphi)} \tag{8}$$

As illustrated in the side schematic of the deposition profile, Eq. (8) is valid for slope angles $\theta > \varphi$. For cases where $\theta \leq \varphi$, the deposition angle exceeds the slope angle. This leads to an unlimited deposition length, which is then controlled primarily by the available material supply.

Fig. 10 shows a comparison between the observed deposition results and the newly proposed theoretical prediction. The horizontal axis represents the normalised tree spacing as appeared in Eq. (8), while the vertical axis is indicated by a normalised slope angle. Observed depositions are classified as "long deposition" and "short deposition", corresponding to lengths greater and smaller than the longitudinal tree spacing, respectively. The theoretical curve predicted by Eq. (8) shows that the normalised slope angle decreases with increasing normalised tree spacing. This trend arises because a larger tree spacing requires a gentler slope to produce a sufficiently long deposition which would result in the deposition length to exceed the longitudinal tree spacing.

Despite the inherent model simplifications, the theoretical prediction agrees well with the experimental observations. The overall agreement suggests that this simple theoretical model provides a reasonable basis for characterising the retention capacity of forests against landslides dominated by fine-grained material. For landslides dominated by coarse-grained material, grain size plays a critical role in forest retention, particularly across varying tree spacings, and thus requires an alternative criterion to characterise forest retention capacity.

Forest retention of coarse-grained landslides

Fig. 11 shows the final deposition profiles of 7-mm gravels at a normalised tree spacing $s/d = 2.9$ under different slope angles: $\theta = 32°$ (Fig. 11a), 36° (Fig. 11b), and 40° (Fig. 11c). The two distinct jamming processes induced by the frontal deposits and arching are indicated in the figure legend. An inset in Fig. 11a highlights the arching in an enlarged view, where the grains are solely supported by the two trees and the slope, without any contact with downstream deposits. Arching consistently forms across the examined slope angles, suggesting the dominant role of tree spacing in arching formation. When the slope increases from 36° to 40°, the deposition pattern shows no significant change. However, a further increase to 45° results in a substantial enlargement of the final deposition area, because the higher flow inertia prolongs the time required to reach equilibrium. Compared with the sand deposits shown in Fig. 7, the gravel deposits exhibit a much more non-uniform pattern, with isolated grains or clusters accumulating behind individual trees. This heterogeneity is primarily attributed to the more complex jamming behaviour in coarse-grained flows, where grain size effects and inter-grain collisions play a more dominant role.

Fig. 12 compares the retention efficiency of gravel within forests under different normalised tree spacings (s/d) and slope angles. At a slope angle of $\theta/\varphi = 0.9$, the forest achieves over 95% retention for tree spacings up to $s/d = 5.7$. As the spacing increases to $s/d = 8.6$, the retention efficiency decreases to 55%, followed by a recovery to 91% at $s/d = 10.0$. With a similar transverse blockage ratio, the different increasing trend in retention efficiency as s/d increases from 8.6 to 10.0 is mainly attributed to the increase in the ratio between tree diameter and grain size (D/d). Similar behavior has been reported for dual-slit check dams (Goodwin and Choi 2020; Huang et al. 2023), where the slit separation plays a role analogous to the tree diameter. DEM simulations show that a larger ratio of separation length to grain size reduces the disturbance between adjacent

openings and leads to higher retention efficiency (Goodwin and Choi 2020). Huang et al. (2023) further demonstrated that stronger force chains develop as the ratio of separation length to grain size increases from 1 to 4, accompanied by increasing retention efficiency. Consistent with these findings, the larger D/d at s/d = 10.0 is expected to promote more stable force chains between adjacent openings in the flow around the trees, as illustrated by the schematic insets in Fig. 12.

When s/d further increases to 15.0, the combined effect of the larger spacing-to-grain-size ratio and the relatively high slope angle (exceeding the interface friction angle) results in only 3% of the material being retained. When the slope angle increases to 36° (θ/φ = 1.0), the same level of full retention as that at θ = 32° is observed for $s/d \leq 5.0$. However, as s/d increases to 5.7, the retention efficiency sharply drops to 57% and becomes negligible at larger spacings. For steeper slopes, the retention efficiency consistently decreases with increasing s/d and remains lower than that on gentler slopes. These results clearly demonstrate the combined influence of slope angle and normalised tree spacing (s/d) on the retention efficiency.

Phase diagram for coarse-grained landslide deposition

The jamming cases were determined if a continuous deposition zone was formed at the end of the impact process. The threshold values of the identified governing parameters required for jamming of coarse grains can be determined using a phase diagram. Fig. 13 shows the observed final gravel depositions with a distinction of jamming (solid symbols) and unjamming (hollow symbols) cases within a two-dimensional parametric space defined by the normalised tree spacing (s/d) and the normalised slope angle (θ/φ). Based on the experimental observations, the jamming and unjamming regions are identified. Within the jamming region, where both slope angle and tree spacing are even smaller, an area of nearly complete retention ($E \geq 95\%$) is achieved, as outlined by the dashed boundary in the figure.

The unjamming conditions exhibiting self-cleaning behaviour in open-type structures with single (Marchelli et al. 2020) and dual (Goodwin and Choi 2020) slits are also included for comparison. The results indicate that slit structures require smaller normalised spacings and slope angles to reach the unjamming regime. This is because a forest contains many more rows of obstacles, which collectively promote jamming. In contrast, unjamming is more likely to occur in slit structures due to their lower levels of confinement.

The transition from jamming to unjamming for a forest is primarily induced by the competition between gravitational driving forces and the mechanical constraints imposed by the trees, which are characterised by the normalised slope angle and normalised tree spacing, respectively. At small tree spacings or gentle slopes, the grains accumulate and interlock between trees, promoting arching and frictional stabilisation that collectively lead to jamming. As the slope angle increases or the tree spacing widens, the enhanced downslope component of gravity and reduced lateral confinement hinder the grain accumulation and formation of stable arching, thereby facilitating unjamming and continued flow. The identified jamming–unjamming boundary thus represents a critical balance between grain inertia, frictional resistance, and geometric confinement. This boundary provides a mechanistic criterion for assessing the retention capacity of forests under different slopes and spacings and may serve as a basis for designing forest configurations in mitigating coarse-grained landslides.

It should be noted that the influence of the normalised tree diameter (D/d) on the jamming threshold is not explicitly represented in Fig. 13. In this study, D/d ranges from 3 to 5 for the coarse-grained flow. As discussed in Fig. 12, a larger D/d can reduce local shearing around the tree and increase retention efficiency, thereby promoting jamming. Accordingly, the predicted jamming region may expand for $D/d > 5$ and shrink for $D/d < 3$.

The proposed phase diagrams could also be used for calibrating numerical model and conducting parametric studies to investigate how tree arrangement, grain polydispersity and the fluid phase affect jamming thresholds, thereby increasing confidence in field-scale applications. The idealised granular materials used in this study enable straightforward calibration or validation of existing discrete element models (Berry et al. 2023), as well as continuum-based modelling frameworks. For example, recent studies have demonstrated that the Lattice Boltzmann Method (Pasqua et al. 2025), the Material Point Method (Ng et al. 2024), and Smoothed Particle Hydrodynamics (Wang and Wu 2024) can model dry granular flows with good fidelity using state-of-the-art $\mu(I)$ rheology, although jamming severely challenges the models.

Conclusions

This study experimentally investigated the interaction mechanisms between landslides and forests, focusing on the effects of grain size, tree spacing, and slope angle on landslide mobility, deposition, and retention. New phase diagrams for characterising the deposition of fine-grained (sand) and coarse-grained (gravel) materials by forests are proposed and validated by the experimental results. Key findings are summarised as follows:

Tree spacing and flow inertia act jointly to govern the onset of energy dissipation. A regularly patterned forest may not effectively impede landslide motion along the flow flanks when preferential flow paths develop. This arrangement allows bow shocks generated at the flanks to bypass effective interaction with downstream trees. By introducing spatial randomness into the forest layout, this could help disrupt preferential paths and thereby enhance the overall energy-dissipation capacity of the forest.

The retention efficiency for fine-grained flows is governed by the combined effects of slope angle and transverse blockage ratio. A simple theoretical model is proposed to predict the threshold condition for continuous deposition induced by jamming. Despite its simplifications, the model shows good agreement with experimental results, providing a useful basis for evaluating the retention capacity of forest against landslides containing a majority of small particle sizes

The deposition of coarse-grained flows is governed by two jamming mechanisms, which are frontal deposit-induced jamming and arching-induced jamming. Frontal deposit-induced jamming was prevalent in all the jamming cases, whereas arching-induced jamming only occurred when $s/d \leq 3$. A phase diagram based on normalised tree spacing by grain size (s/d) and normalised slope angle by angle of repose (θ/φ) may serve to delineate the threshold between jamming and unjamming regimes.

Design takeaways follow directly from the phase diagrams. For fine-grained flows, achieving continuous deposition, and therefore strong retention, requires jointly satisfying a slope condition and a blockage condition, increasing stem density alone is insufficient at steep slopes. For coarse-grained flows, frontal deposit-induced jamming can occur across a wider range, but arching-induced jamming is only expected when tree spacing is smaller than about three grain diameters. This provides a clear spacing rule tied to grain size. Regular stem layouts can also create low resistance flank corridors, so introducing controlled spatial variability is a practical way to reduce preferential paths.

Overall, the findings demonstrate that landslide mobility and forest retention capacity are strongly grain-size dependent. Fine-grained materials are effectively retained through enhanced energy dissipation and continuous deposition, while coarse-grained materials experience geometric confinement and interlocking which leads to jamming. The phase diagrams established in this

study offer a scientific and practical basis for predicting forest performance and optimising forest configurations for landslide mitigation.

The proposed thresholds are intended as screening rules derived from controlled dry granular flows and simplified rigid stems, within the tested Froude number range and material properties. Extension to saturated debris flows, deformable vegetation, entrainment, and breakage will require additional testing and modelling, but the dimensionless framing offers a direct route for those extensions.

Acknowledgements

This work was financially supported by the UK Engineering and Physical Sciences Research Council (EPSRC), under grant number UKRI179, titled “Rooting for Resilience: Forests as physical barriers to landslide runout”. The authors express their gratitude to Mr Aaron Benson, who helped collecting preliminary data.

References

Benito, J., Bertho, Y., Ippolito, I., Gondret, P., 2012. Stability of a granular layer on an inclined “fakir plane”. Europhys. Lett. 100(3), 34004. https://doi.org/10.1209/0295-5075/100/34004

Berry, N., Zhang, Y., Haeri, S., 2023. Contact models for the multi-sphere discrete element method. Powder Technol. 416, 118209. https://doi.org/10.1016/j.powtec.2022.118209

Booth, A.M., Sifford, C., Vascik, B., Siebert, C., Buma, B., 2020. Large wood inhibits debris flow runout in forested southeast Alaska. Earth Surf. Process. Landf. 45(7), 1555–1568. https://doi.org/10.1002/esp.4830

Cagnoli, B., 2024. Flow front mobility of rock avalanches as a function of flow volume, grain size, channel width, basal friction and flow scale. Landslides 21(5), 933–947. https://doi.org/10.1007/s10346-023-02190-9

Choi, C.E., 2025. The 3rd Hutchinson lecture: Numerical modelling of forests with uprooting as a nature-based solution to mitigate flow-type landslides. Landslides 22, 2883–2896. https://doi.org/10.1007/s10346-024-02388-5

Choi, C.E., Ng, C.W.W., Song, D., Kwan, J.H.S., Shiu, H.Y.K., Ho, K.K.S., Koo, R.C., 2014. Flume investigation of landslide debris–resisting baffles. Can. Geotech. J. 51(5), 540–553. https://doi.org/10.1139/cgj-2013-0115

Choi, C.E., Goodwin, G.R., Ng, C.W.W., Cheung, D.K.H., Kwan, J.S.H., Pun, W.K., 2016. Coarse granular flow interaction with slit structures. Géotech. Lett. 6(4), 267–274. https://doi.org/10.1680/jgele.16.00103

Choi, C.E., Ng, C.W.W., Liu, H., Wang, Y., 2020. Interaction between dry granular flow and a rigid barrier with basal clearance: analytical and physical modelling. Can. Geotech. J. 57(2), 236–245. https://doi.org/10.1139/cgj-2018-0622

Cui, X., Gray, J.M.N.T., 2013. Gravity-driven granular free-surface flow around a circular cylinder. J. Fluid Mech. 720, 314–337. https://doi.org/10.1017/jfm.2013.42

Cui, Y., Choi, C.E., Liu, L.H., Ng, C.W., 2018. Effects of particle size of mono-disperse granular flows impacting a rigid barrier. Nat. Hazards 91(3), 1179–1201. https://doi.org/10.1007/s11069-018-3185-3

Cui, Y., Fang, J., Li, Y., Liu, H., 2022. Assessing effectiveness of a dual-barrier system for mitigating granular flow hazards through a DEM–DNN framework. Eng. Geol. 306, 106742. https://doi.org/10.1016/j.enggeo.2022.106742

Darbois Texier, B., Bertho, Y., Gondret, P., 2023. Downslope granular flow through a forest of obstacles. Phys. Rev. Fluids 8, 034303. https://doi.org/10.1103/PhysRevFluids.8.034303

Fang, J., Cui, Y., Liu, H., Zhang, L., Zhou, G.G., Fan, H., 2023. Influences of deposition upslope of the barrier on the dynamic impact of dry granular flow. Eng. Geol. 323, 107212. https://doi.org/10.1016/j.enggeo.2023.107212

Fidan, S., Tanyaş, H., Akbaş, A., Lombardo, L., Petley, D.N., Görüm, T., 2024. Understanding fatal landslides at global scales: A summary of topographic, climatic, and anthropogenic perspectives. Nat. Hazards 120, 6437–6455. https://doi.org/10.1007/s11069-024-06487-3

Froude, M.J., Petley, D.N., 2018. Global fatal landslide occurrence from 2004 to 2016. Nat. Hazards Earth Syst. Sci. 18, 2161–2181. https://doi.org/10.5194/nhess-18-2161-2018

Goodwin, S.R., Choi, C.E., 2020. Slit structures: Fundamental mechanisms of mechanical trapping of granular flows. Comput. Geotech. 119, 103376. https://doi.org/10.1016/j.compgeo.2019.103376

Huang, Y., Bi, Y., Zhang, B., 2023. DEM investigation of the interaction between rapid dry granular flow and dual-slit structures. Eng. Geol. 313, 106957. https://doi.org/10.1016/j.enggeo.2022.106957

Iverson, R.M., Logan, M., Denlinger, R.P., 2004. Granular avalanches across irregular three-dimensional terrain: 2. Experimental tests. J. Geophys. Res. Earth Surf. 109(F1), F01015. https://doi.org/10.1029/2003JF000084

Jan, C.D., Nguyen, L.T., Dey, L., 2025a. Effects of grain size distribution on the movement and deposition of granular materials flowing down an inclined channel. J. Mech. 41, 157–172. https://doi.org/10.1093/jom/ufaf012

Jan, C.D., Zeng, Y.C., Dey, L., 2025b. Numerical simulation of debris flow behavior over a series of groundsills. Water 17(3), 293. https://doi.org/10.3390/w17030293

Jerolmack, D.J., Daniels, K.E., 2019. Viewing Earth's surface as a soft-matter landscape. Nat. Rev. Phys. 1, 716–730. https://doi.org/10.1038/s42254-019-0111-x

Johnson, C.G., Kokelaar, B.P., Iverson, R.M., Logan, M., LaHusen, R.G., Gray, J.M.N.T., 2012. Grain-size segregation and levee formation in geophysical mass flows. J. Geophys. Res. Earth Surf. 117(F1), F01032. https://doi.org/10.1029/2011JF002185

Jop, P., Forterre, Y., Pouliquen, O., 2006. A constitutive law for dense granular flows. Nature, 441(7094), 727–730. https://doi.org/10.1038/nature04801

Khan, A., Verma, S., Hankare, P., Kumar, R., Kumar, S., 2020. Shock–shock interactions in granular flows. J. Fluid Mech. 884, R4. https://doi.org/10.1017/jfm.2019.988

Kong, Y., Li, X., Zhao, J., 2021. Quantifying the transition of impact mechanisms of geophysical flows against flexible barriers. Eng. Geol. 289, 106188. https://doi.org/10.1016/j.enggeo.2021.106188

Kong, Y., Guan, M., 2023. Hydro-mechanical simulations aid demand-oriented design of slit dams for controlling debris flows, debris avalanches and rock avalanches. Eng. Geol. 326, 107314. https://doi.org/10.1016/j.enggeo.2023.107314

Leonardi, A., Goodwin, S.R., Pirulli, M., 2019. The force exerted by granular flows on slit dams. Acta Geotech. 14(6), 1949–1963. https://doi.org/10.1007/s11440-019-00842-6

Liang, Z., Choi, C.E., Zhao, Y., Jiang, Y., Choo, J., 2023. Revealing the role of forests in the mobility of geophysical flows. Comput. Geotech. 155, 105194. https://doi.org/10.1016/j.compgeo.2022.105194

Luong, T.H., Baker, J.L., Einav, I., 2020. Spread-out and slow-down of granular flows through model forests. Granul. Matter 22(1), 15. https://doi.org/10.1007/s10035-019-0980-9

Marchelli, M., Leonardi, A., Pirulli, M., Scavia, C., 2020. On the efficiency of slit-check dams in retaining granular flows. Géotechnique 70(3), 226–237. https://doi.org/10.1680/jgeot.18.P.044

Nedderman, R.M., 1992. *Statics and Kinematics of Granular Materials*. Cambridge University Press, Cambridge, 352 pp.

Ng, C.W.W., Choi, C.E., Song, D., Kwan, J.H.S., Koo, R.C.H., Shiu, H.Y.K., Ho, K.K.S., 2015. Physical modeling of baffles influence on landslide debris mobility. Landslides 12(1), 1–18. https://doi.org/10.1007/s10346-014-0476-y

Ng, C.W.W., Choi, C.E., Liu, H., Poudyal, S., Kwan, J.S.H., 2020. Design recommendations for single and dual debris flow barriers with and without basal clearance. In: Sassa, K. et al. (Eds.), Understanding and Reducing Landslide Disaster Risk: Volume 1, Sendai Landslide

Partnerships and Kyoto Landslide Commitment 5th. Springer, Cham, Switzerland, pp. 33–53. https://doi.org/10.1007/978-3-030-60196-6_2

Ng, C.W.W., Jia, Z., Poudyal, S., Bhatta, A., Liu, H., 2024. Two-phase MPM modelling of debris flow impact against dual rigid barriers. Géotechnique 74(12), 1390–1403. https://doi.org/10.1680/jgeot.22.00199

Nicoll, B., 2016. Agriculture and Forestry Climate Change Report Card Technical Paper 8: Risks for Woodlands, Forest Management and Forestry Production in the UK from Climate Change. Living With Environmental Change (LWEC) Network, 1–34. https://www.ukri.org/wpcontent/uploads/2021/12/131221-NERC-LWEC-AgricultureForestrySource8-RisksWoodlands.pdf

Pasqua, A., Leonardi, A., Pirulli, M., 2025. A multiscale framework for simulating landslide runout and impact with barriers. Can. Geotech. J. 62, 1–19. https://doi.org/10.1139/cgj-2025-0034

Perzl, F., Bono, A., Garbarino, M., Motta, R., 2021. Protective effects of forests against gravitational natural hazards. In: Teich, M., Accastello, C., Perzl, F., Kleemayr, K. (Eds.), Protective Forests as Ecosystem-based Solutions for Disaster Risk Reduction (Eco-DRR). IntechOpen, London. https://www.intechopen.com/online-first/77984

Piton, G., Goodwin, S.R., Mark, E., Strouth, A., 2022. Debris flows, boulders and constrictions: a simple framework for modelling jamming and its consequences on outflow. J. Geophys. Res. Earth Surf. 127(5), e2021JF006447. https://doi.org/10.1029/2021JF006447

Stoffel, M., Mendlik, T., Schneuwly-Bollschweiler, M., Gobiet, A., 2014. Possible impacts of climate change on debris-flow activity in the Swiss Alps. Clim. Change 122(1), 141–155. https://doi.org/10.1007/s10584-013-0993-z

Song, D., Chen, X., Zhou, G.G., Lu, X., Cheng, G., Chen, Q., 2021. Impact dynamics of debris flow against a rigid obstacle in laboratory experiments. Eng. Geol. 291, 106211. https://doi.org/10.1016/j.enggeo.2021.106211

Song, D., Zhou, G.G.D., Xu, M., Choi, C.E., Li, S., Zheng, Y., 2019. Quantitative analysis of debris-flow flexible barrier capacity from momentum and energy perspectives. Eng. Geol. 251, 81–92. https://doi.org/10.1016/j.enggeo.2019.02.010

Thielicke, W., 2014. The flapping flight of birds: Analysis and application. Ph.D. thesis, University of Groningen, Groningen, the Netherlands.

Thielicke, W., Stamhuis, E.J., 2014. PIVlab – toward user-friendly, affordable and accurate digital particle image velocimetry in MATLAB. J. Open Res. Softw. 2, e30. https://doi.org/10.5334/jors.bl

To, K., Lai, P.-Y., Pak, H.K., 2001. Jamming of granular flow in a two-dimensional hopper. Phys. Rev. Lett. 86(1), 71–74. https://doi.org/10.1103/PhysRevLett.86.71

van den Broek, A.J., Mennes, D.T., Kleinhans, M.G., Roelofs, L., Eichel, J., Draebing, D., de Haas, T., 2026. Impacts of plant roots on debris-flow bed erosion in laboratory experiments. Eng. Geol. 362, 108513. https://doi.org/10.1016/j.enggeo.2025.108513

Védrine, L., Li, X., Gaume, J., 2022. Detrainment and braking of snow avalanches interacting with forests. Nat. Hazards Earth Syst. Sci. 22(3), 1015–1028. https://doi.org/10.5194/nhess-22-1015-2022

Wang, Y., Wu, W., 2025. A SPH model bridging solid- and fluid-like behaviour in granular materials. Int. J. Numer. Anal. Methods Geomech. 49(2), 738–755. https://doi.org/10.1002/nag.3899

Yanites, B.J., Clark, M.K., Roering, J.J., West, A.J., Zekkos, D., Baldwin, J.W., Cerovski-Darriau, C., Gallen, S.F., Horton, D.E., Kirby, E., Leshchinsky, B.A., 2025. Cascading land surface hazards as a nexus in the Earth system. Science 388(6754), eadp9559. https://doi.org/10.1126/science.adp9559

Zhang, W., Wang, X., Hong, X., Chen, S., Ji, J., Gao, Y., 2024. Run-out distance analysis and impact force estimation for an actual landslide with a multiple-barrier system based on a coupled SPH model. Comput. Geotech. 170, 106330. https://doi.org/10.1016/j.compgeo.2024.106330

Zhou, G.G.D., Hu, H.S., Song, D., Zhao, T., Chen, X.Q., 2019. Experimental study on the regulation function of slit dam against debris flows. Landslides, 16(1), 75–90. https://doi.org/10.1007/s10346-018-1065-2

Zhou, G.G.D., Du, J., Song, D., Choi, C.E., Hu, H.S., Jiang, C., 2020. Numerical study of granular debris flow run-up against slit dams using the discrete element method. Landslides 17(3), 585–595. https://doi.org/10.1007/s10346-019-01287-4

Fig. 1. Field photos from a landslide site near the A83 road in Scotland, UK, showing coarse-grained deposits behind (a) a single tree and (b) multiple trees.

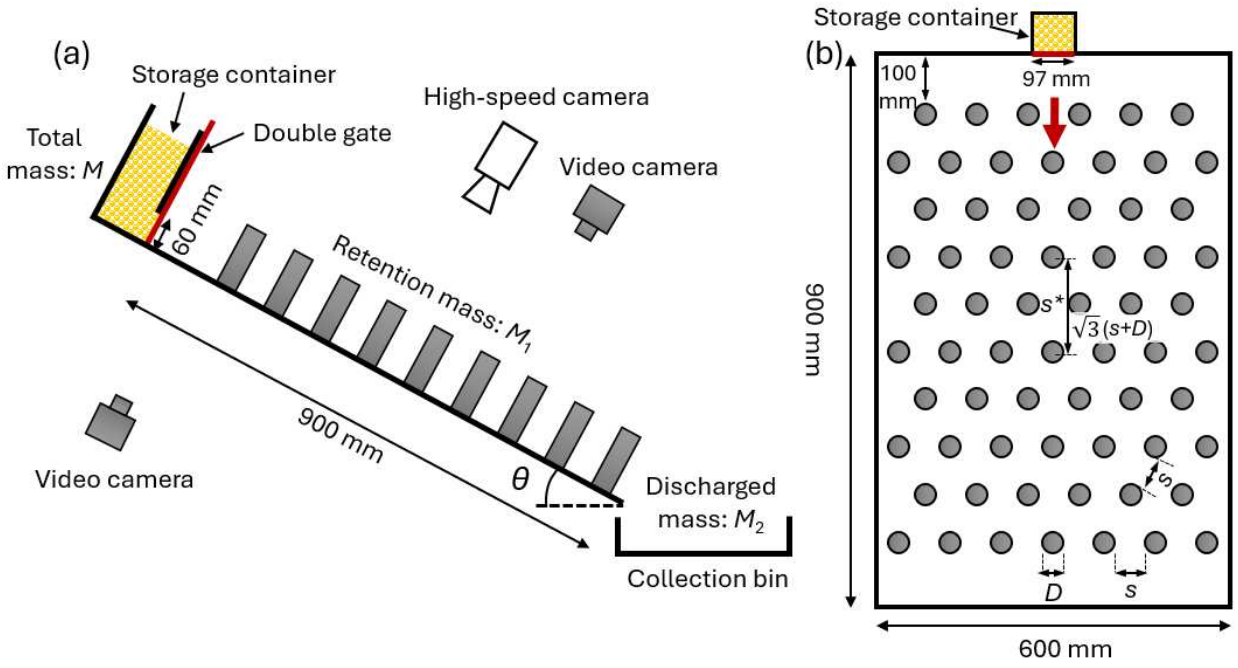

Fig. 2. Schematic of the experimental setup: (a) side view; (b) top view.

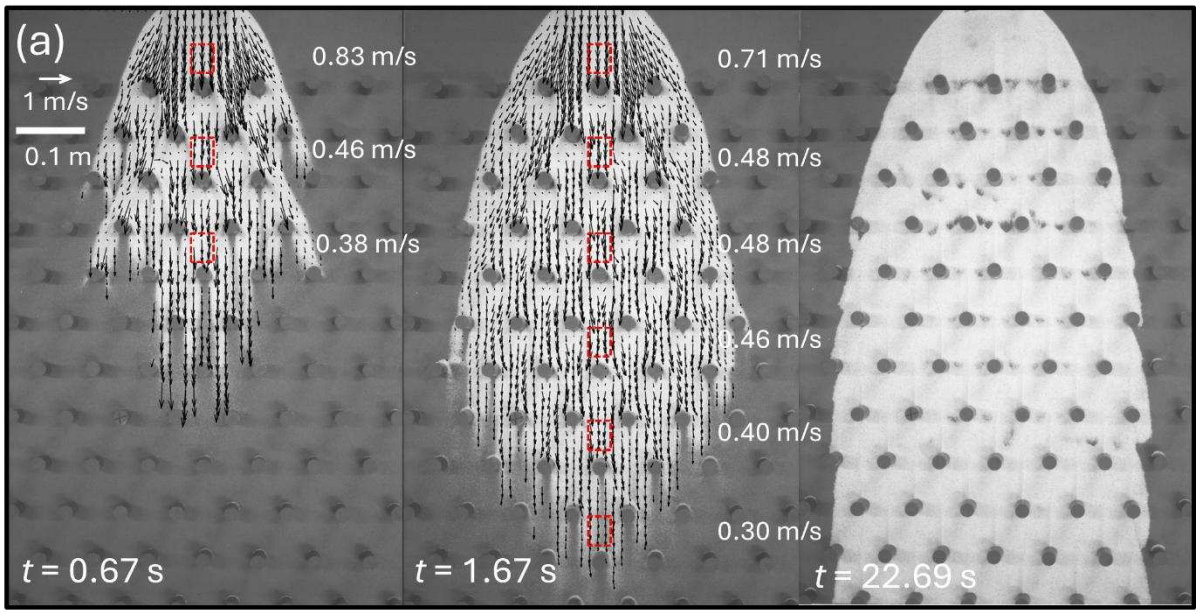
(a)
1 m/s
0.1 m
0.83 m/s
0.46 m/s
0.38 m/s
0.71 m/s
0.48 m/s
0.48 m/s
0.46 m/s
0.40 m/s
0.30 m/s
t = 0.67 s
t = 1.67 s
t = 22.69 s

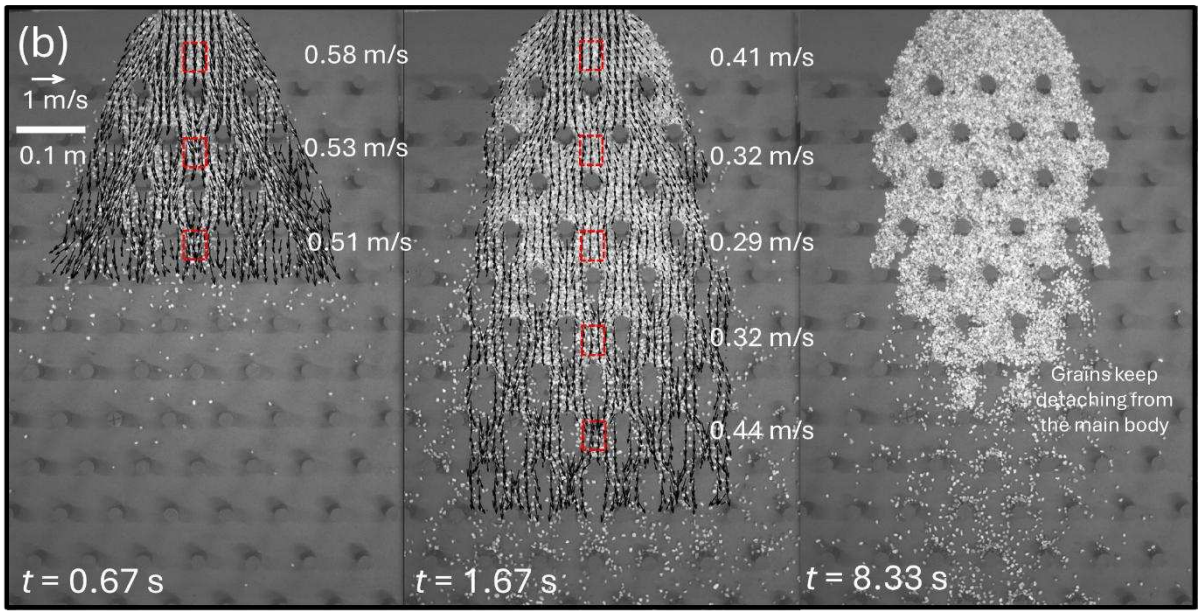
(b)
1 m/s
0.1 m
0.58 m/s
0.53 m/s
0.51 m/s
0.41 m/s
0.32 m/s
0.29 m/s
0.32 m/s
0.44 m/s
Grains keep detaching from the main body
t = 0.67 s
t = 1.67 s
t = 8.33 s

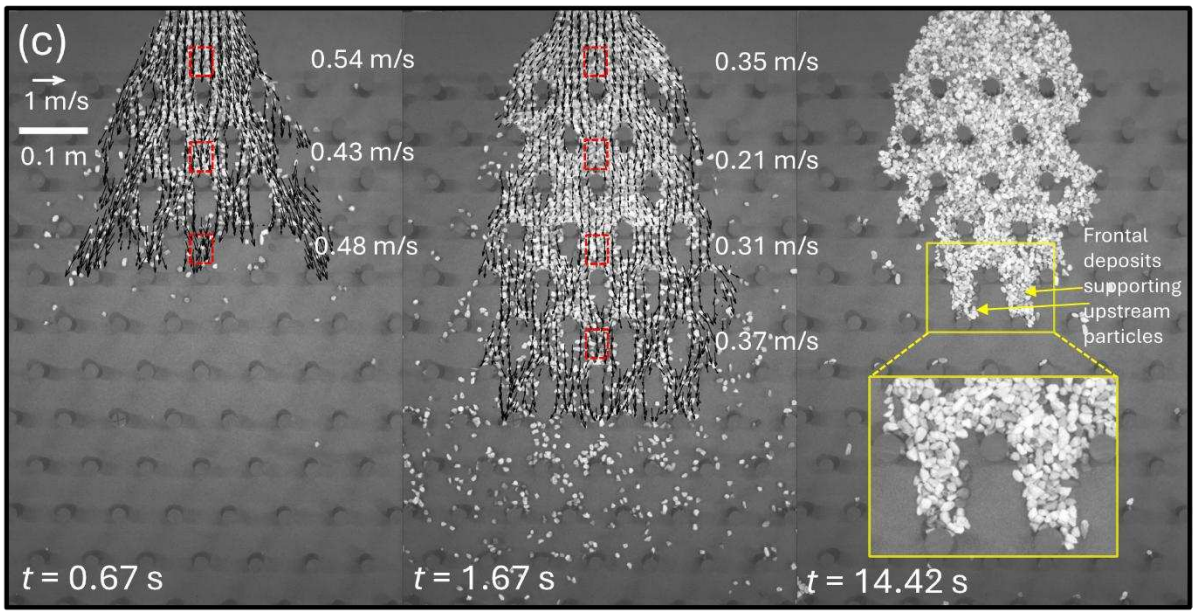

Fig. 3. Impact kinematics captured by the high-speed camera with particle image velocimetry (PIV) analysis for tests on a 32° slope with a tree spacing of 60 mm and varying grain sizes: (a) fine-grained flow with sand; (b) coarse-grained flow with 4-mm gravel (*s/d* = 15.0); (c) coarse-grained flow with 7-mm gravel (*s/d* = 8.6).

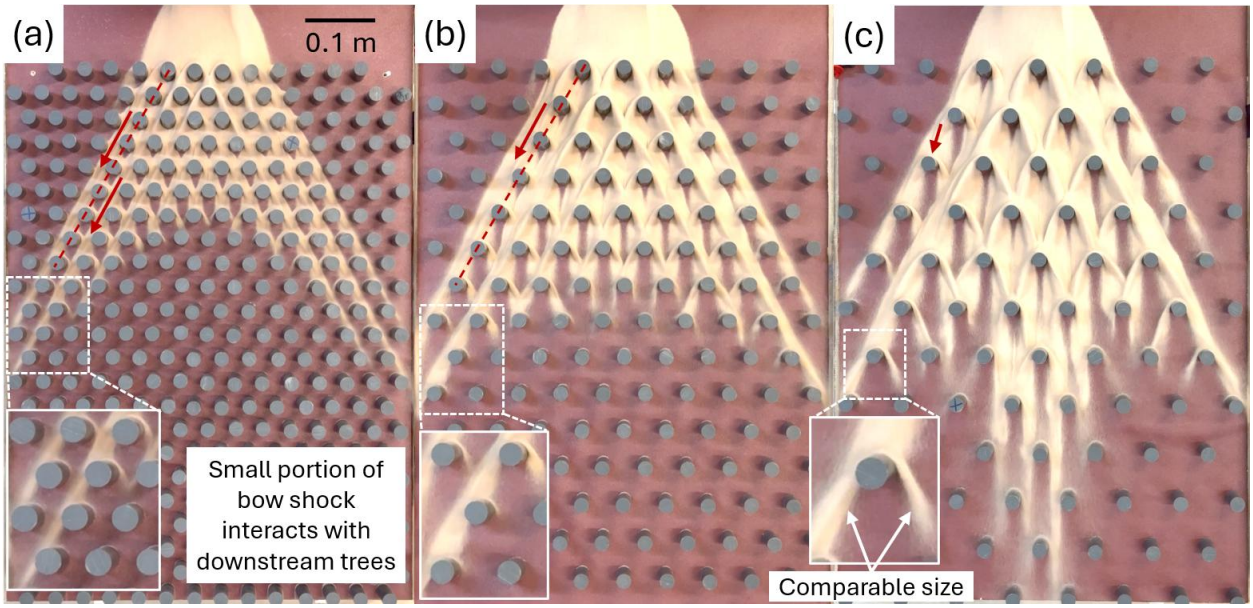

Fig. 4. Flow-front propagation of fine-grained flow on a 45° slope for different tree spacings at the moment when the lateral flow reaches the sidewalls: (a) *s* = 20 mm; (b) *s* = 40 mm; (c) *s* = 60 mm.

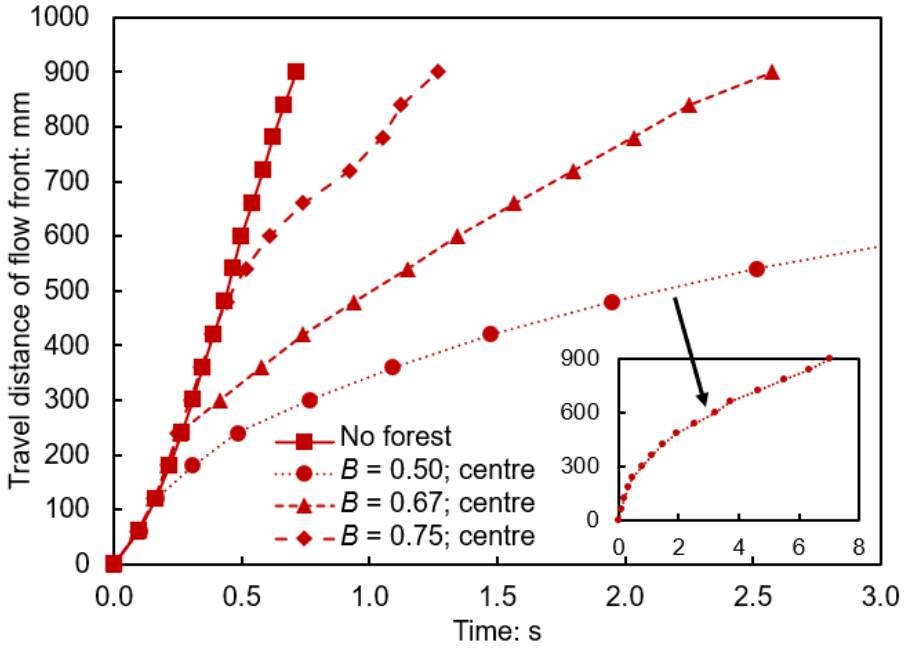

(a)

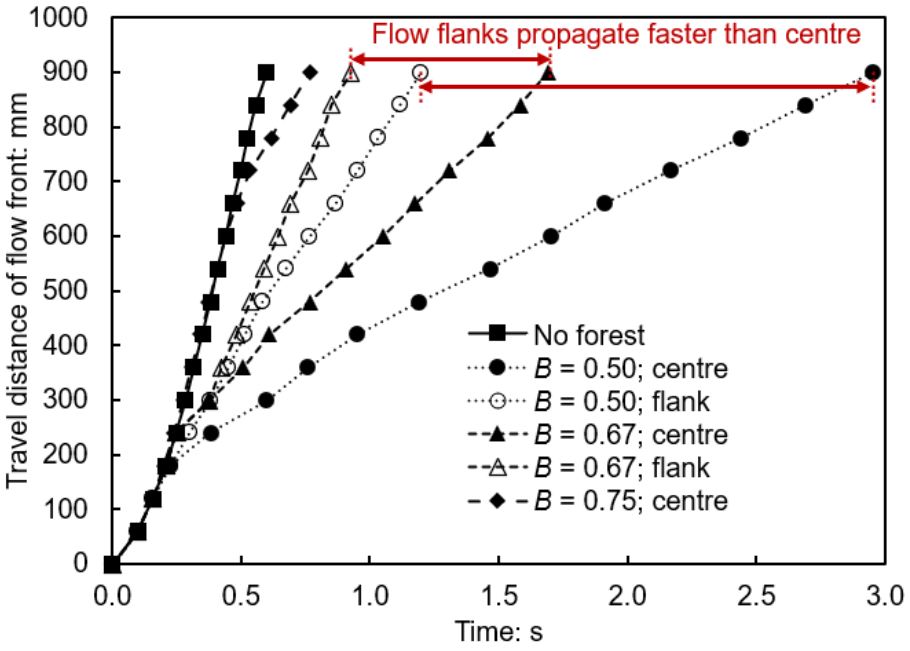

(b)

Fig. 5. Time history of the travel distance of flow front under different transverse blockage ratios and slope angles: (a) θ = 36°; (b) θ = 45°.

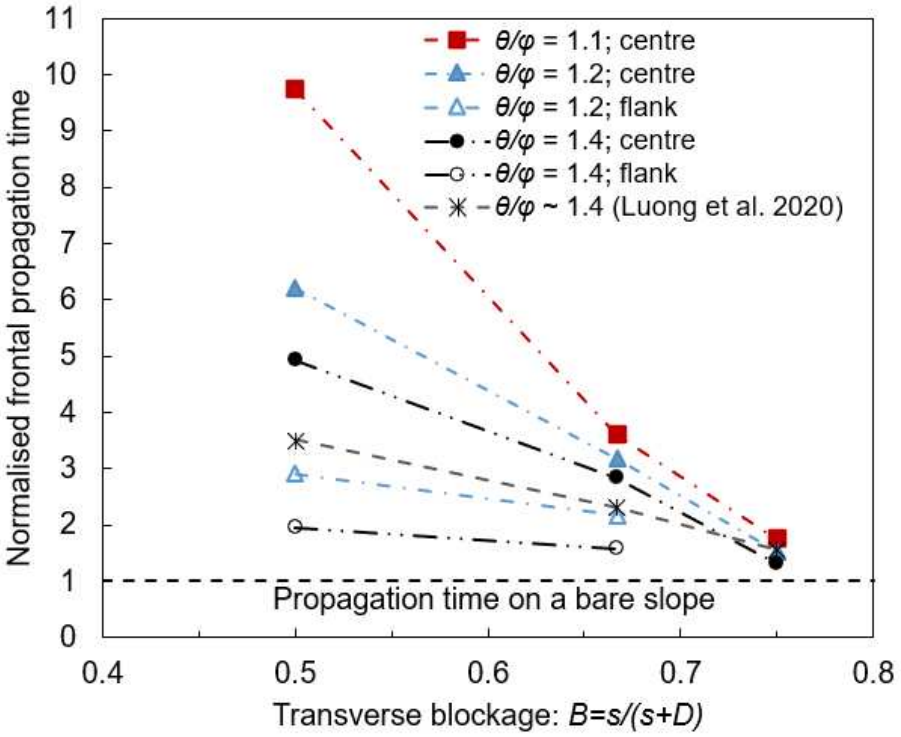

Fig. 6. Normalised propagation time of the fine-grained flow front across slopes with forests of varying transverse blockage ratios.

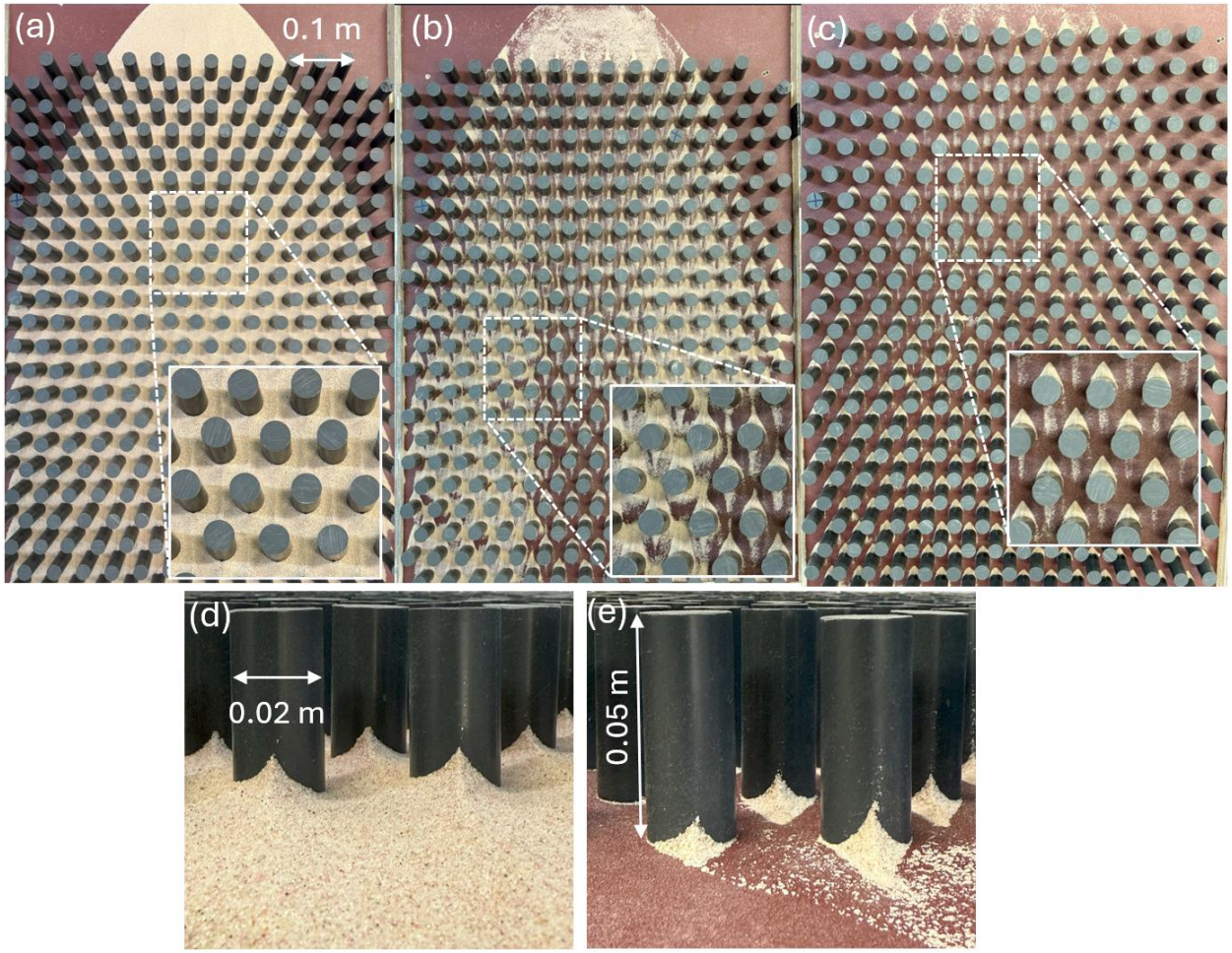

Fig. 7. Final deposition profiles of fine-grained flow for tests with a transverse blockage of 0.5 at different slope angles: (a) 36°; (b) 40°; (c) 45°; and closer front views showing (d) long deposition and (e) short deposition.

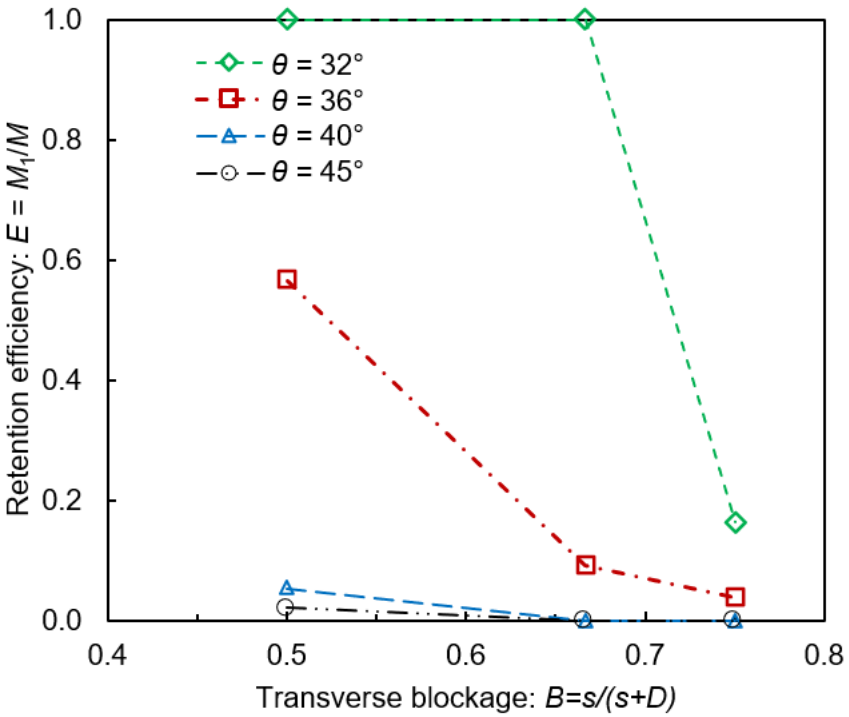

Fig. 8. Retention efficiency of fine-grained flow for different normalised tree spacings and slope angles.

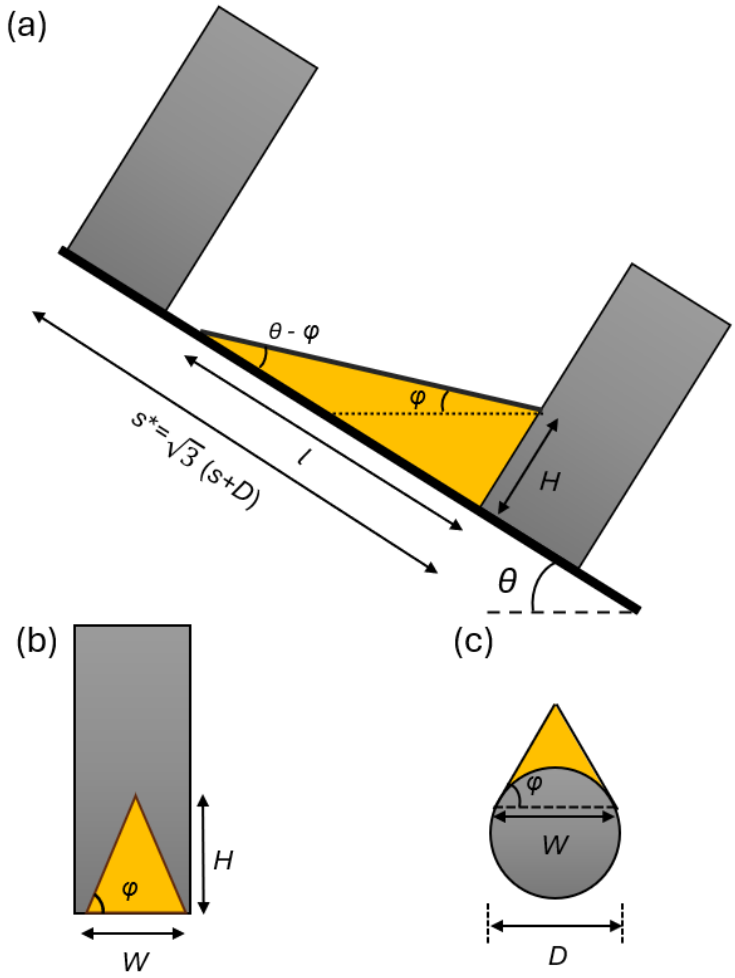

Fig. 9. Idealised deposition profiles of fine-grained flow against a single tree: (a) side view of deposition along the slope; (b) front view of deposition on the tree surface; and (c) top view of deposition along the cylindrical tree element surface.

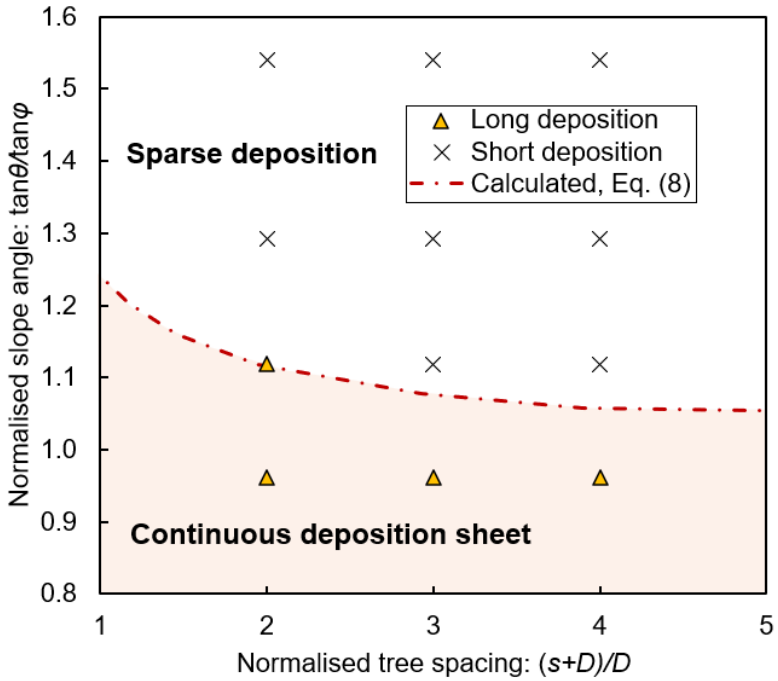

Fig. 10. Comparison between observed cases of long and short depositions and the theoretical prediction for fine-grained flow.

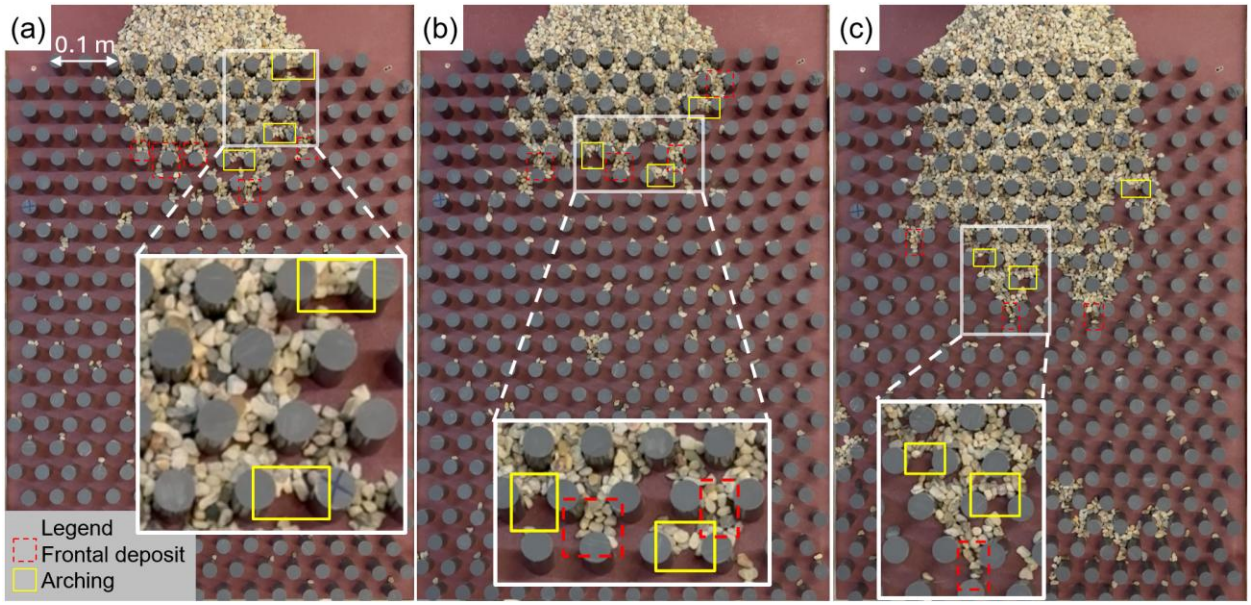

Fig. 11. Final deposition profiles of coarse-grained flow using 7-mm gravel for tests with a normalised tree spacing (*s/d*) of 2.9 at different slope angles: (a) 36°; (b) 40°; and (c) 45°.

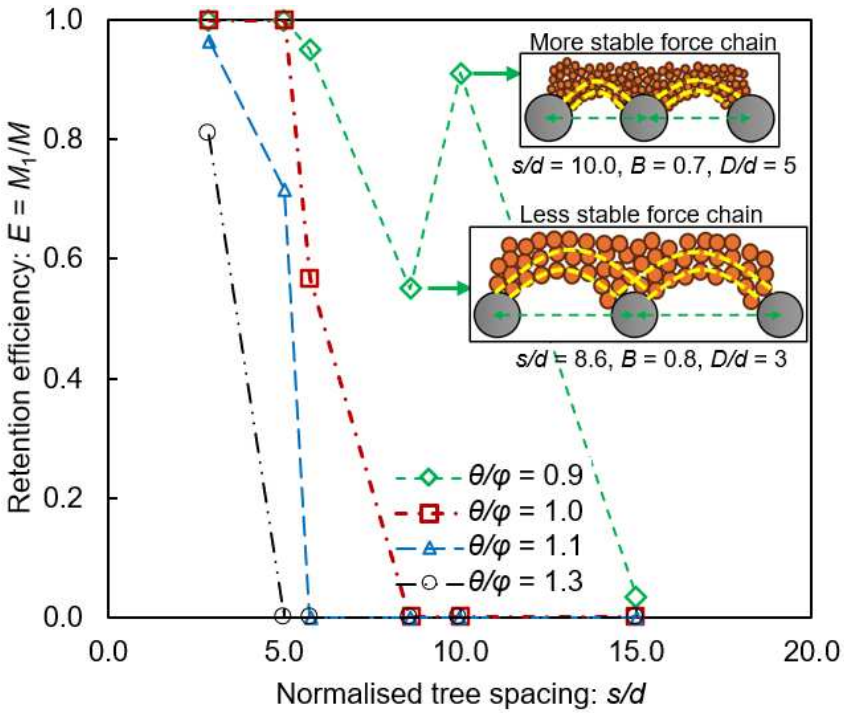

Fig. 12. Retention efficiency of coarse-grained flows for different normalised tree spacings and slope angles. The inset schematics illustrate force-chain development as the flow impacts the forest under different transverse blockage ratios (B) and tree-diameter-to-grain-size ratios (D/d). A smaller D/d may lead to less stable force chains owing to stronger interference between adjacent force-chain networks.

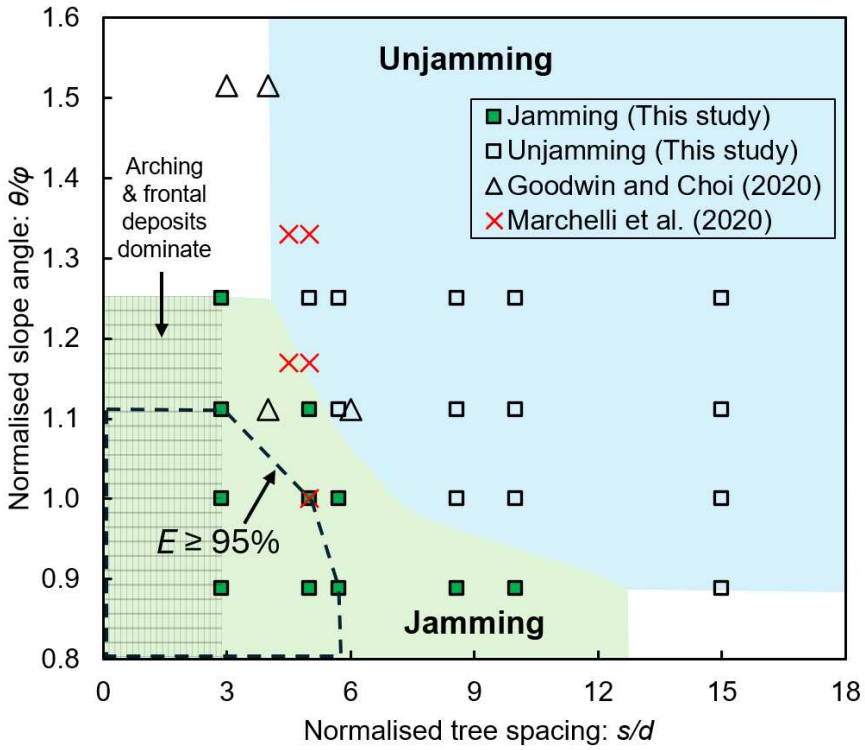

Fig. 13. Phase diagram of the observed final deposition of coarse-grained flow. Unjamming cases exhibiting self-cleaning behaviour in open-type structures with single (Marchelli et al. 2020) and dual (Goodwin and Choi 2020) slits are included for comparison. The grid area in the jamming region indicates jamming induced by both arching and frontal deposits, whereas the rest of the jamming region is only induced by frontal deposits.